Optimizing Proton Stopping Power Ratio Prediction with Dual-Energy Cone-Beam CT Using the Cramér-Rao Lower Bound

Leibold, David; Schaart, Dennis R.; Goorden, Marlies C.

DOI
10.1117/12.3006731

Publication date
2024

Document Version
Final published version

Published in
Medical Imaging 2024

Optimizing Proton Stopping Power Ratio Prediction with Dual-Energy Cone-Beam CT Using the Cramér-Rao Lower Bound

David Leibold[a], Dennis R. Schaart[a,b], Marlies C. Goorden[a]
[a]Department of Radiation Science and Technology, Delft University of Technology, Delft, The Netherlands
[b]Holland Proton Therapy Center, Delft, The Netherlands

ABSTRACT

Cone-beam computed tomography (CBCT) and X-ray projection radiography are commonly used in the proton therapy workflow for the verification of patient positioning. The prospect of using the CBCT images for dose calculation purposes is attractive but currently hampered by the poorer image quality compared to the planning (fan-beam) CT. Ideally, the CBCT scan with the patient's anatomy of the day would provide sufficiently accurate proton stopping power ratios (SPR) to directly replan the treatment if needed. Dual-energy fan-beam CT has been proven to increase the accuracy of calculated SPR values compared to single-energy CT. A similar outcome may therefore be expected for dual-energy/spectral CBCT. This work aims to compare two possible realizations of dual-energy CBCT, namely a rapid kVp-switching source CBCT and a photon-counting detector (PCD) CBCT with two energy bins, with respect to their suitability for extracting SPR values. To perform this comparison, we determine the Cramér-Rao Lower Bound on the variance of the estimated electron density and effective atomic number. In our simulation study, we find that for the rapid kVp-switching setup the optimum voltage pair is 80/140 kVp, and the optimum ratio of the source current at 80 kVp to the source current at 140 kVp is 2:1 (4:1) for extracting the electron density (effective atomic number). In case of the PCD-based setup, a 140 kVp (100 kVp) spectrum and energy bins of [20; 50), [50; 150) keV appear best suited for extracting electron density (effective atomic number), outperforming the kVp-switching setup by a factor of 3.8 (4.9).

Keywords: Spectral cone-beam CT, dual-energy CBCT, proton therapy, stopping power ratio, SPR, Cramér-Rao Lower Bound.

1 INTRODUCTION

Proton therapy offers the possible advantage of sparing healthy tissue by depositing a large portion of its dose in the small volume of the Bragg peak.[1,2] At the same time, this raises the requirements on the accuracy needed for a safe delivery of radiation dose. A pivotal aspect of meeting this requirement is a precise knowledge of the proton stopping power ratio (SPR) in order to accurately steer the beam within the patient's body.

In the current proton therapy workflow, a planning X-ray fan-beam CT is performed prior to the start of a treatment series, which can be either a single-energy or a dual-energy CT scan. This planning CT serves as the basis for delineating the tumor as well as organs-at-risk, and for extracting SPR values. Just prior to each treatment session, daily cone-beam CT (CBCT) or projection radiographs are commonly acquired to determine the patient's position on the patient bed. If a significant mismatch between the patient's anatomy of the day and the patient's anatomy during the planning CT is discovered, this may trigger a re-planning, which commonly requires a new planning CT. Otherwise, the last treatment plan is used to irradiate the patient.

The proton therapy workflow could be significantly improved if an anatomical mismatch detected via CBCT didn't require a new planning CT scan, but simply triggered an update of the treatment plan based on the already available CBCT images. While warping the original planning CT images, and hence the SPR values, to the anatomy of the day as registered by the CBCT scan is currently used as an alternative,[3–6] this introduces additional uncertainties; the direct use of the daily CBCT scan is therefore preferrable. However, the image quality of CBCT is currently inferior to that of fan-beam CT due to the fact that CBCT is more susceptible to scatter,[7] beam hardening, detector lag[8] and patient movement, which hampers its application as the basis for continuous treatment plan updates.

Medical Imaging 2024: Physics of Medical Imaging, edited by Rebecca Fahrig, John M. Sabol, Ke Li,
Proc. of SPIE Vol. 12925, 129253N · © 2024 SPIE · 1605-7422
doi: 10.1117/12.3006731

One route to enhance CBCT image quality could be by using the principle of dual-energy imaging. In the case of fan-beam CT it has already been demonstrated that the accuracy of SPR values can be improved by using dual-energy instead of single-energy CT:[9,10] while the conversion between CT numbers (i.e., X-ray attenuation) obtained from a single-energy scan to SPR values is based on an empirical method called the Schneider conversion,[11] this might yield incorrect results for some materials since two materials can have the same X-ray attenuation yet different chemical composition, and therefore different SPR values.

In contrast to a single-energy scan that can at most yield one physical quantity, a dual-energy scan is capable of yielding two physical parameters, where one of them might be an indication of chemical composition. A common choice is the electron density, ρ_{elec}, and the effective atomic number, Z_{eff}.[12–14] While the relationship between SPR on the one hand and ρ_{elec} and Z_{eff} on the other is not trivial, we argue that an X-ray scan that can extract ρ_{elec} and Z_{eff} with the highest accuracy will enable the most accurate prediction of SPR as well.

Furthermore, since dual-energy X-ray imaging can provide information about the chemical composition, this additional information could help to better distinguish between different tissues and thus help with tumor or organs-at-risk delineation.[15,16]

Two possible ways of realizing dual-energy CBCT are considered in this work, namely (1) a setup using a single rapid voltage-switching X-ray tube and a single energy-integrating detector (also known as 'rapid kVp-switching (CB)CT'), as well as (2) a setup using a source operating at a constant voltage and a photon-counting detector (PCD) with two energy bins. In this work, we will compare the above-mentioned possible realizations of dual-energy CBCT with respect to their aptitude of extracting ρ_{elec} and Z_{eff} of the object under investigation. We will assume perfect detectors with 100 % detection efficiency and perfect spectral separation, since these are technological limitations, not fundamental physical limits. Our figure of merit will be the Cramér-Rao Lower Bound (CRLB) on the variance of ρ_{elec} and Z_{eff}. Although scatter is a main cause of inferior image quality of CBCT compared to CT, the inclusion of this effect requires computationally expensive Monte-Carlo (MC) simulations of particle transport. We will therefore first optimize the parameters of the setup with a semi-analytical model similar to preceding studies such as the one conducted by Roessl and Herrmann;[17] MC simulations including scatter are subsequently used to validate the semi-analytical results and investigate the effects of scatter.

2 METHODOLOGY

2.1 Rationale

We aim to compare the two dual-energy CBCT modalities in projection space in order to assess the inherent information content of the acquired data without depending on the performance of the reconstruction algorithm. To do so, we employ the statistical framework of the CRLB, which yields the minimum variance achievable by an unbiased estimator of a parameter of interest (here, ρ_{elec} or Z_{eff}) from an observed distribution, without requiring the knowledge of an explicit analytical formula for the relationship between the parameter of interest and the observed distribution.

We argue that a fair comparison between setups and setup parameters is based on how well a parameter of interest can be extracted given the same dose to the patient or object. Vice versa, the best performing setup can extract the parameter of interest with a set quality using the lowest dose. Hence, we kept the cumulative energy deposited in the object constant at an arbitrary value of 30.085 ± 0.011 GeV. This dose was chosen since it could be achieved in our MC simulation with reasonable computational effort. Furthermore, we don't expect the chosen absolute dose value to have an influence on the assessment obtained via the CRLB.

Since MC simulations are computationally very demanding, a semi-analytical approach was employed to investigate which settings (i.e., current ratios, source voltages, energy bins) yield the best performance. Finally, the computationally demanding MC simulation was run for the optimum parameters to investigate the influence of scatter.

2.2 CRLB formalism

This section closely follows Steven M. Kay's chapter on the CRLB theory.[18] Let $f(\boldsymbol{x}|\boldsymbol{\theta})$ be the probability density function (PDF) of a measurement $\boldsymbol{x}$ depending on a parameter vector $\boldsymbol{\theta}$ which we wish to estimate. The variance of any unbiased estimator $\widehat{\boldsymbol{\theta}}$ of $\boldsymbol{\theta}$ is then bound by the CRLB, which equals the inverse of the Fisher information matrix. If the PDF of $\boldsymbol{x}$ is

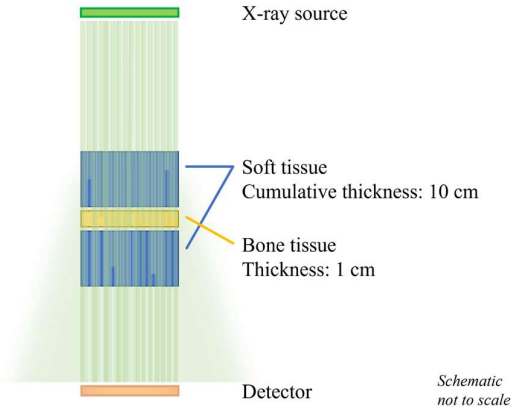

Figure 1: Schematic of the simulated setup: The X-ray source emits a parallel beam of X-rays, which passes through a total of 10 cm of soft tissue as well as 1 cm bone (for compositions see appendix). The Monte-Carlo simulation incorporates a realistic scatter model, whereas the semi-analytical approach based on the Lambert-Beer law does not model the scatter component incident on the detector.

a multivariate normal distribution with mean $\boldsymbol{m}(\boldsymbol{\theta})$ and covariance matrix $\boldsymbol{\Sigma}(\boldsymbol{\theta})$, the entries of the Fisher information $\boldsymbol{I}(\boldsymbol{\theta})$ matrix can be calculated according to (Kay[18], Eq. 3.31):

$$[\boldsymbol{I}(\boldsymbol{\theta})]_{ij} = \left[\frac{\partial \boldsymbol{m}(\boldsymbol{\theta})}{\partial \theta_i}\right]^T \boldsymbol{\Sigma}^{-1}(\boldsymbol{\theta}) \left[\frac{\partial \boldsymbol{m}(\boldsymbol{\theta})}{\partial \theta_j}\right] + \frac{1}{2}\mathrm{tr}\left[\boldsymbol{\Sigma}^{-1}(\boldsymbol{\theta})\frac{\partial \boldsymbol{\Sigma}(\boldsymbol{\theta})}{\partial \theta_i}\boldsymbol{\Sigma}^{-1}(\boldsymbol{\theta})\frac{\partial \boldsymbol{\Sigma}(\boldsymbol{\theta})}{\partial \theta_j}\right] \quad (1)$$

The CRLB then states that the lower limit for the variance of any unbiased estimator $\hat{\theta}_i$ of θ_i is $\mathrm{Var}\left[\hat{\theta}_i\right] \geq [\boldsymbol{I}^{-1}(\boldsymbol{\theta})]_{ii}$. In our case, the entries of the parameter vector $\boldsymbol{\theta}$ correspond to the electron density ρ_{elec} and the effective atomic number Z_{eff}, and the entries of $\boldsymbol{x}$ correspond to the two measurements, either the deposited energy in the detector at different source voltages (kVp setup) or the number of photons in different energy bins (PCD setup).

The derivatives were numerically evaluated by running the simulation at points θ_i, $\theta_i \pm \Delta\theta_i$ and $\theta_i \pm 2\Delta\theta_i$, changing one component at a time while keeping all others fixed, and using the five-point method for calculating the first derivative: Let g be a function of θ_i, then $g'(\theta_i) = \left(-g(\theta_i + 2\Delta\theta_i) + 8g(\theta_i + \Delta\theta_i) - 8g(\theta_i - \Delta\theta_i) + g(\theta_i - 2\Delta\theta_i)\right)/(12 \cdot \Delta\theta_i)$.

2.3 Object and material definitions

The object consists of slabs of, in total, 10 cm soft tissue and 1 cm bone, which are traversed by the X-ray beam on its way from the source to the detector. The soft tissue slab was split into two equally thick slabs of 5 cm, surrounding the bone insert (see Figure 1).

In order to determine the sensitivity of the various implementations of dual-energy CBCT w.r.t. ρ_{elec} and Z_{eff} using CRLB, one parameter needs to be varied while keeping the other fixed so that the partial derivatives $\partial/\partial\theta_i$ can be evaluated. We chose to vary the elemental composition and electron density of the soft tissue insert by about 1 %, while keeping the specifications of the bone insert fixed. The bone insert was modelled according to adult cortical bone as specified in the ICRU report[19] 44 (see Table A1). For further details we refer to Appendix A.

The effective atomic number Z_{eff} was calculated according to the following formula:

$$Z_{\mathrm{eff}} = \left(\frac{\sum_i f_i \cdot Z_i^{n+1} / A_i}{\sum_i f_i \cdot Z_i / A_i}\right)^{1/n}, \quad (2)$$

Where f_i, Z_i and A_i denote the weight fraction, the atomic number and the atomic mass of constituent i, respectively, with $n = 3.1$ (based on Hünemohr *et al.*[20]).

2.4 Monte-Carlo approach

The MC simulation was implemented using GATE (version 9.2),[21] which is based on the GEANT4 toolkit[22] (version 11.0.0). The source, phantom and detector all have dimensions of 363 × 264 mm, and the X-rays were simulated as a parallel beam to allow for a direct comparison with the semi-analytical approach (see below). The source-isocenter distance is 2300 mm, the isocenter-detector distance 900 mm. For both setups (kVp-switching and PCD), the detector is modelled as an idealized detector, registering all incident particles. The registered photons were split into scattered and non-scattered photons based on their trajectory. If they intersected the detector plane at a position that was more than 0.1 mm apart from the expected intersection point, calculated based on the emission point on the source, they were flagged as scattered photons. As a result, the MC approach yields two datasets, one with and one without the scatter component on the detector.

The MC simulation used to calculate the CRLB sampled the probability distribution of the resulting signal $\boldsymbol{x}$ 6600 times; this was repeated 3 times in order to obtain a standard deviation on the CRLB. Please note that in case of the MC simulation of the PCD setup, the application of the energy binning is done in post-processing of the data, always using the same underlying dataset.

The MC simulation was furthermore used to determine the number of photons needed to achieve the desired reference value of deposited energy in the phantom to enable a fair comparison between all setups.

2.5 Semi-analytical approach

For the given object composition we calculated the line integral analytically, based on attenuation coefficients extracted from the Xraydb library[23] (version 4.4.7) for a range of energies in steps of 1 keV. Using the Lambert-Beer law and the spectral fluence rate of a particular source spectrum, this yields the expected number of photons per keV incident on the detector. We then apply Poisson sampling to this expected number of photons to generate a sample of the probability distribution. Please note that, first, this approach assumes a parallel beam, and, second, it neglects the contribution of scattered photons to the detector signal. Furthermore, the number of photons emitted by the source is set to the same value as in the MC approach.

In case of the semi-analytical model used to calculate the CRLB for the PCD setup, the probability distribution of the resulting signal $\boldsymbol{x}$ was sampled $4.8 \cdot 10^6$ times. In case of the semi-analytical model used to calculate the CRLB for the kVp-switching setup, the $f(\boldsymbol{x}|\boldsymbol{\theta})$ was sampled $4.8 \cdot 10^5$ times. In both cases, the procedure was repeated five times to obtain the standard deviation on the CRLB.

2.6 Details on the dual-energy CBCT realizations

One rapid voltage-switching source and one energy-integrating detector: It is assumed that the energy-integrating detector exhibits perfect energy resolution and 100 % detection efficiency; neither pixel-crosstalk nor electronic noise is included. The investigated voltage pairs are 80/140, 80/120, 100/140 and 120/140 kVp, all filtered by 0.8 mm Be and 0.89 mm Ti.

One source operating at a constant voltage and one photon-counting detector with two energy bins: It is assumed that the PCD possesses perfect energy resolution and 100 % detection efficiency. Neither pixel-crosstalk, pile-up, nor electronic noise is included. The PCD outputs the number of photons that are registered in each energy bin. The bottom threshold of the lower energy bin is fixed at 20 keV and the upper threshold of the higher energy bin is fixed at 150 keV (note that all events have an energy lower than 150 keV since pile-up is neglected). The compared spectra are based on a 80, 100, 120 and 140 kVp source voltage, all filtered with 0.8 mm Be and 0.89 mm Ti.

We simulated the X-ray spectra using SPEKCALC[24] for a tungsten target and an anode angle of 30° with energy steps of 1 keV.

3 RESULTS AND DISCUSSION

For the kVp-switching setup, both the choice of the low/high source voltage pair as well as the ratio between the source currents for the low/high energy spectra were optimized using the semi-analytical model due to its lower computational demands. See Table B1 for the number of photons emitted by the source for each source voltage pair and current ratio in

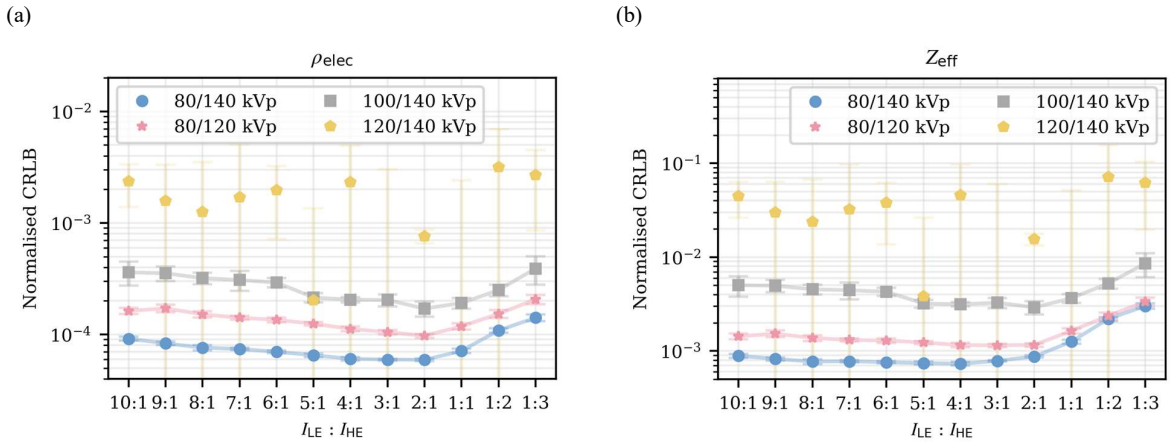

Figure 2: Normalized CRLB values for estimating ρ_{elec} (a) and Z_{eff} (b) as achieved by the kVp-switching setup for different ratios between the source current of the low energy spectrum (I_{LE}) and the source current of the high energy spectrum (I_{HE}) while keeping the deposited energy fixed. All results were obtained using the semi-analytical approach. All values are normalized by the electron density/effective atomic number of the material under investigation.

order to reach the desired cumulative (i.e., combined low and high energy spectrum) deposited target energy in the phantom.

Figure 2 shows the CLRB as achieved by the kVp-switching setup for estimating the soft tissue's ρ_{elec} (Fig. 2a) and Z_{eff} (Fig. 2b) using different source voltage pairs (80/140, 100/140, 120/140, 80/120 kVp) and different ratios between the source currents of the low energy spectrum (I_{LE}) and the high energy spectrum (I_{HE}). The lowest CRLB for an unbiased estimator of ρ_{elec} is achieved for a 80/140 kVp voltage pair and a current ratio (I_{LE}:I_{HE}) of 2:1, whereas the lowest CRLB for an unbiased estimator of Z_{eff} is achieved for the same voltage pair but a current ratio (I_{LE}:I_{HE}) of 4:1, hence putting a larger weight on the information contained in the low-energy spectrum. We would like to note that the CRLB calculation for the 120/140 kVp voltage pair was numerically unstable, sometimes yielding even negative values (negative values are not shown in Figure 2). Please note that all CRLB values were normalized by the electron density/effective atomic number of the material under investigation (i.e., soft tissue at $\theta_{Z_{eff}}$, see Table A1 and Section 2.3).

Since in the MC simulation the photons were split into scattered and non-scattered photons, we can compare the MC simulation to the semi-analytical approach and furthermore investigate the influence of scatter on the results (Table 1). A Welch's unequal variances *t*-test shows that the results obtained by the semi-analytical and the MC approach are statistically

Table 1: Normalized CRLB values for estimating ρ_{elec} and Z_{eff} as achieved by the kVp-switching setup using an 80/140 kVp voltage pair, obtained via the semi-analytical and MC approach, and based on the optimum parameters as obtained from the semi-analytical approach. All values are normalized by the electron density/effective atomic number of the material under investigation.

	Normalized CRLB for estimating ρ_{elec}, I_{LE}:I_{HE} = 2:1	Normalized CRLB for estimating Z_{eff}, I_{LE}:I_{HE} = 4:1
Semi-analytical model, excluding scatter	$(5.91 \pm 0.16) \cdot 10^{-5}$	$(7.31 \pm 0.30) \cdot 10^{-4}$
MC simulation, excluding scatter	$(5.27 \pm 0.28) \cdot 10^{-5}$	$(6.90 \pm 0.48) \cdot 10^{-4}$
MC simulation, including scatter	$(4.35 \pm 0.17) \cdot 10^{-5}$	$(7.60 \pm 0.40) \cdot 10^{-4}$

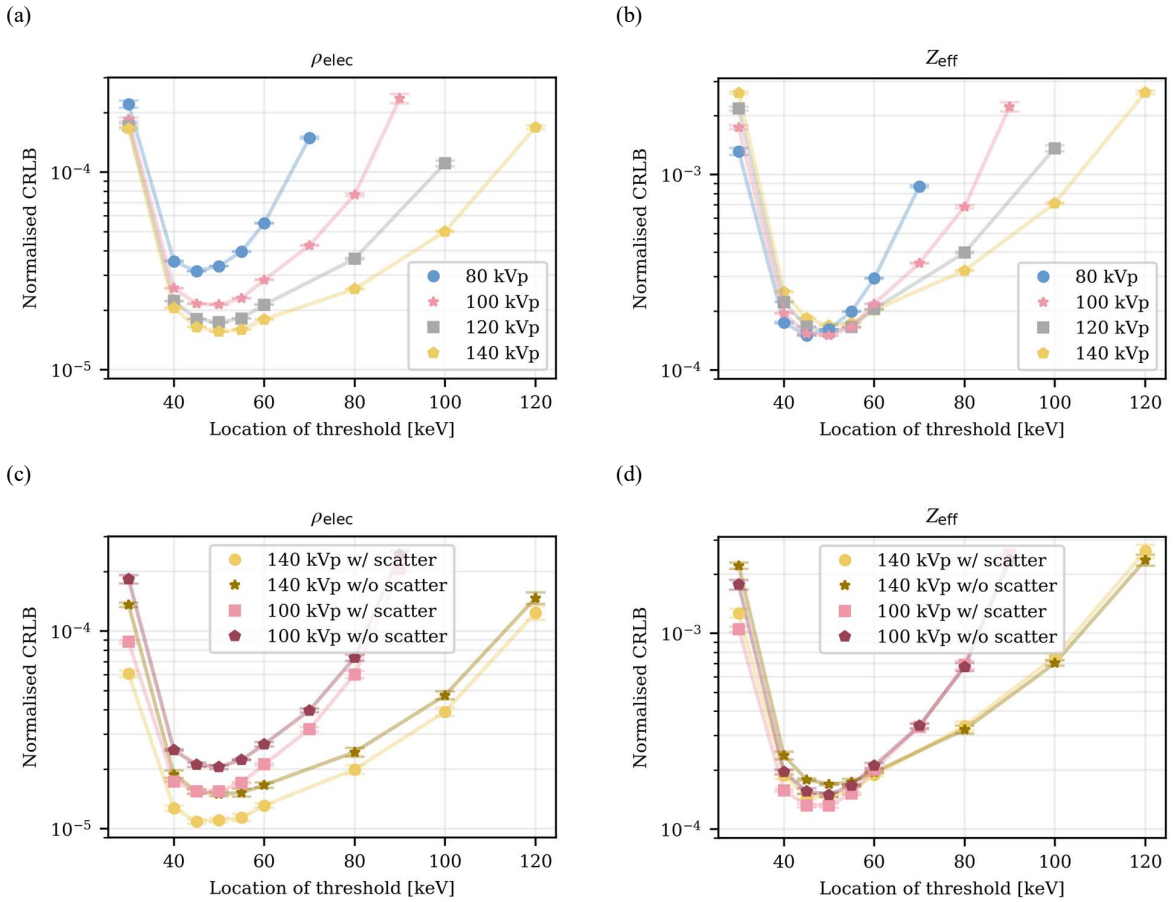

Figure 3: Normalized CRLB values for estimating ρ_{elec} (a, c) and Z_{eff} (b, d) as achieved by the PCD setup for different values of the threshold between the low- and high-energy bin while keeping the deposited energy fixed. (a) and (b) were obtained using the semi-analytical approach, (c) and (d) using the Monte-Carlo simulation (with/without scatter). All values are normalized by the electron density/effective atomic number of the material under investigation.

equal for both extracting ρ_{elec} and Z_{eff}. A comparison of the MC results with and without scatter shows that adding the scatter component lowers the CRLB in case of estimating ρ_{elec}, but increases it for Z_{eff}. The fact that scatter can improve the extraction of a parameter at all might seem counter-intuitive, but can most likely be attributed to the simplifications applied to the geometry in our MC simulation. We would like to remind the reader that our setup essentially mimics a single macro-pixel, which is different from a realistic setup where one might be interested in the change of a line integral along a single ray ℓ between source and detector, while keeping the remainder of the phantom fixed. In this case, most of the scatter will originate from outside ray ℓ, and a change in the line integral along ℓ will not change the amount of scatter received by the detector significantly. In our situation of a macro-pixel and varying the whole phantom's composition, however, a change in the line integral will also change the received scatter component, and since the scatter component also carries information about the line integral it might help lower the CRLB.

For the PCD setup, both the threshold between the lower and higher energy bin was optimized, as well as the employed X-ray spectrum. See Table B2 for the number of photons emitted by the source for each source spectrum in order to reach the desired deposited target energy in the phantom.

Figure 3a and 3b show the CLRB, calculated using the semi-analytical approach, as achieved by the PCD setup for estimating ρ_{elec} (Fig. 3a) and Z_{eff} (Fig. 3b) using different source voltages (80, 100, 120 and 140 kVp) and different thresholds between the low and high energy bin. The lowest CRLB for ρ_{elec} is achieved for a 140 kVp spectrum and an energy bin threshold of 50 keV (resulting in a lower energy bin with a range of [20; 50) keV and a higher energy bin with

Table 2: Comparison of the lowest normalized CRLB values for estimating ρ_{elec} and Z_{eff} as achieved by either the kVp-switching setup or the PCD setup, as obtained via the semi-analytical approach (hence excluding the influence of scatter). All values are normalized by the electron density/effective atomic number of the material under investigation.

	Parameters for achieving / value of lowest CRLB for estimating ρ_{elec}	Parameters for achieving / value of lowest CRLB for estimating Z_{eff}
kVp-switching setup	80/140 kVp, I_{LE}:I_{HE} = 2:1, $(5.91 \pm 0.16) \cdot 10^{-5}$	80/140 kVp, I_{LE}:I_{HE} = 4:1, $(7.31 \pm 0.30) \cdot 10^{-4}$
PCD setup	140 kVp, thrsh. at 50 keV, $(1.5549 \pm 0.0037) \cdot 10^{-5}$	100 kVp, thrsh. at 50 keV, $(1.4977 \pm 0.0045) \cdot 10^{-4}$
Ratio $CRLB_{kVp}$ / $CRLB_{PCD}$	3.8	4.9

a range of [50; 150) keV), whereas the lowest CRLB for Z_{eff} is achieved for a 100 kVp spectrum and the same energy binning. Note that the use of the 80 kVp spectrum and an energy binning of [20; 45) keV, [45; 150) keV yields an almost identical, though slightly larger CRLB.

Based on the semi-analytical results, the MC simulation was run for source voltages of 100 kVp and 140 kVp. We find that in case of extracting ρ_{elec} (Fig. 3c), the added scatter component always lowers the CRLB. In case of extracting Z_{eff} (Fig. 3d), the added scatter component lowers the CRLB for lower values (≤ 60 keV) of the energy bin threshold, but increases it for larger values of the energy bin threshold (≥80 keV).

A comparison between the kVp-switching setup and the PCD setup shows that the latter always outperforms the former (Table 2). The CRLB in case of the kVp-switching setup for estimating ρ_{elec} is about a factor of 3.8 worse compared to the PCD setup, and about a factor of 4.9 worse in case of estimating Z_{eff}.

Evidently, the optimum configuration is different for either extracting electron density or the effective atomic number, where the latter prefers a stronger contribution of the information contained in the low energy spectrum.

4 CONCLUSIONS AND OUTLOOK

In this work, we compared different realizations of dual-energy cone-beam CT with respect to their suitability for extracting proton stopping power ratios. The two investigated setups were (1) a rapid kVp-switching source combined with an energy-integrating detector and (2) a fixed-voltage source combined with a photon-counting detector. For our figure of merit we chose the Cramér-Rao Lower Bound for extracting the electron density and the effective atomic number, which we used as proxies for extracting the proton SPR. To allow for a fair comparison between the two setups, we optimized each w.r.t. the acquisition parameters, i.e., employed source voltage (1, 2), source current setting (1) and thresholds of the energy bins (2), while keeping the deposited energy inside the phantom fixed.

The acquisition parameters were optimized using a semi-analytical approach based on the Lambert-Beer law. For both the rapid kVp-switching setup as well as the PCD setup it is evident that the optimum configuration is different for either extracting electron density or the effective atomic number; the latter prefers a stronger contribution of the information contained in the low energy spectrum. We find that for the investigated task the PCD-based CBCT outperforms the kVp-switching setup by a factor of 3.8 (4.9) w.r.t. extracting electron density (effective atomic number).

For the optimized acquisition parameters of each setup, a Monte-Carlo simulation was used to investigate the effect of scatter. Depending on the parameter to be estimated and the acquisition settings, the inclusion of the scatter signal either lowered or increased the CRLB. The fact that the inclusion of scatter can yield a better CRLB can most likely be attributed to the fact that our MC simulation essentially mimics a macro pixel, due to which a change in object composition also

changes the scattered X-rays received by that macro pixel. This is not representative of a realistic setup, where the majority of scatter received by a pixel will originate from outside the line-of-sight between this detector pixel and the source.

Based on the first results shown in this study, we will employ the same methodology in future studies to cover a broader range of possible dual-energy CBCT implementations, including dual-layer detector setups and dual-source/dual-detector setups. We will also optimize the filtration of the source spectrum, which in this study was kept constant. Last but not least, we will adapt our simulation such that it reflects the effect of the scatter component on the CRLB in a realistic manner.

While in this study we assume ideal detectors (unit detection efficiency, perfect energy resolution, etc.), the same methodology could be applied to compare and optimize detector parameters, determine minimum detector performance requirements and to optimize prototype setups.

In conclusion, we hope that our approach shows potential to investigate and compare various dual-energy CBCT implementations at a reasonable computational cost, and contribute to a more precise proton radiotherapy in the future.

DISCLOSURE

DL is funded in part by Varian, a Siemens Healthineers Company, grant number 2018016.

ACKNOWLEDGEMENTS

DL would like to thank Dan Wang for help with the Cramér-Rao Lower Bound formalism. The authors would like to acknowledge the high-performance computing clusters provided by the ICT department of TU Delft.

REFERENCES

[1] Newhauser, W. D. and Zhang, R., "The physics of proton therapy," Phys. Med. Biol. **60**(8), R155–R209 (2015).

[2] Chen, Z., Dominello, M. M., Joiner, M. C. and Burmeister, J. W., "Proton versus photon radiation therapy: A clinical review," Front. Oncol. **13**, 1133909 (2023).

[3] Rigaud, B., Simon, A., Castelli, J., Lafond, C., Acosta, O., Haigron, P., Cazoulat, G. and De Crevoisier, R., "Deformable image registration for radiation therapy: principle, methods, applications and evaluation," Acta Oncologica **58**(9), 1225–1237 (2019).

[4] Landry, G., Nijhuis, R., Dedes, G., Handrack, J., Thieke, C., Janssens, G., Orban de Xivry, J., Reiner, M., Kamp, F., Wilkens, J. J., Paganelli, C., Riboldi, M., Baroni, G., Ganswindt, U., Belka, C. and Parodi, K., "Investigating CT to CBCT image registration for head and neck proton therapy as a tool for daily dose recalculation," Medical Physics **42**(3), 1354–1366 (2015).

[5] Landry, G., Dedes, G., Zöllner, C., Handrack, J., Janssens, G., Orban De Xivry, J., Reiner, M., Paganelli, C., Riboldi, M., Kamp, F., Söhn, M., Wilkens, J. J., Baroni, G., Belka, C. and Parodi, K., "Phantom based evaluation of CT to CBCT image registration for proton therapy dose recalculation," Phys. Med. Biol. **60**(2), 595–613 (2015).

[6] Kurz, C., Kamp, F., Park, Y.-K., Zöllner, C., Rit, S., Hansen, D., Podesta, M., Sharp, G. C., Li, M., Reiner, M., Hofmaier, J., Neppl, S., Thieke, C., Nijhuis, R., Ganswindt, U., Belka, C., Winey, B. A., Parodi, K. and Landry, G., "Investigating deformable image registration and scatter correction for CBCT-based dose calculation in adaptive IMPT," Medical Physics **43**(10), 5635–5646 (2016).

[7] Siewerdsen, J. H., Daly, M. J., Bakhtiar, B., Moseley, D. J., Richard, S., Keller, H. and Jaffray, D. A., "A simple, direct method for x-ray scatter estimation and correction in digital radiography and cone-beam CT: X-ray scatter correction," Med. Phys. **33**(1), 187–197 (2005).

[8] Tanaka, R., Ichikawa, K., Mori, S., Dobashi, S., Kumagai, M., Kawashima, H., Minohara, S. and Sanada, S., "Investigation on Effect of Image Lag in Fluoroscopic Images Obtained with a Dynamic Flat-panel Detector (FPD) on Accuracy of Target Tracking in Radiotherapy," JRR **51**(6), 723–731 (2010).

[9] Taasti, V. T., Michalak, G. J., Hansen, D. C., Deisher, A. J., Kruse, J. J., Krauss, B., Muren, L. P., Petersen, J. B. B. and McCollough, C. H., "Validation of proton stopping power ratio estimation based on dual energy CT using fresh tissue samples," Phys. Med. Biol. **63**(1), 015012 (2017).

[10] Hünemohr, N., Krauss, B., Dinkel, J., Gillmann, C., Ackermann, B., Jäkel, O. and Greilich, S., "Ion range estimation by using dual energy computed tomography," Zeitschrift für Medizinische Physik **23**(4), 300–313 (2013).
[11] Schneider, U., Pedroni, E. and Lomax, A., "The calibration of CT Hounsfield units for radiotherapy treatment planning," Phys. Med. Biol. **41**(1), 111–124 (1996).
[12] Saito, M. and Sagara, S., "A simple formulation for deriving effective atomic numbers via electron density calibration from dual-energy CT data in the human body," Med. Phys. **44**(6), 2293–2303 (2017).
[13] Landry, G., Seco, J., Gaudreault, M. and Verhaegen, F., "Deriving effective atomic numbers from DECT based on a parameterization of the ratio of high and low linear attenuation coefficients," Phys. Med. Biol. **58**(19), 6851–6866 (2013).
[14] Li, B., Lee, H. C., Duan, X., Shen, C., Zhou, L., Jia, X. and Yang, M., "Comprehensive analysis of proton range uncertainties related to stopping-power-ratio estimation using dual-energy CT imaging," Phys. Med. Biol. **62**(17), 7056–7074 (2017).
[15] Bazalova, M., Carrier, J.-F., Beaulieu, L. and Verhaegen, F., "Dual-energy CT-based material extraction for tissue segmentation in Monte Carlo dose calculations," Phys. Med. Biol. **53**(9), 2439–2456 (2008).
[16] Landry, G., Granton, P. V., Reniers, B., Öllers, M. C., Beaulieu, L., Wildberger, J. E. and Verhaegen, F., "Simulation study on potential accuracy gains from dual energy CT tissue segmentation for low-energy brachytherapy Monte Carlo dose calculations," Phys. Med. Biol. **56**(19), 6257–6278 (2011).
[17] Roessl, E. and Herrmann, C., "Cramér–Rao lower bound of basis image noise in multiple-energy x-ray imaging," Phys. Med. Biol. **54**(5), 1307–1318 (2009).
[18] Steven M Kay., [Fundamentals of statistical signal processing: estimation theory], Prentice-Hall, Inc. (1993).
[19] White, D. R., Booz, J., Griffith, R. V., Spokas, J. J. and Wilson, I. J., "Report 44," Journal of the International Commission on Radiation Units and Measurements **os23**(1), NP-NP (1989).
[20] Hünemohr, N., Krauss, B., Tremmel, C., Ackermann, B., Jäkel, O. and Greilich, S., "Experimental verification of ion stopping power prediction from dual energy CT data in tissue surrogates," Phys. Med. Biol. **59**(1), 83–96 (2014).
[21] Sarrut, D., Bardiès, M., Boussion, N., Freud, N., Jan, S., Létang, J.-M., Loudos, G., Maigne, L., Marcatili, S., Mauxion, T., Papadimitroulas, P., Perrot, Y., Pietrzyk, U., Robert, C., Schaart, D. R., Visvikis, D. and Buvat, I., "A review of the use and potential of the GATE Monte Carlo simulation code for radiation therapy and dosimetry applications: GATE for dosimetry," Med. Phys. **41**(6Part1), 064301 (2014).
[22] Allison, J., Amako, K., Apostolakis, J., Arce, P., Asai, M., Aso, T., Bagli, E., Bagulya, A., Banerjee, S., Barrand, G., Beck, B. R., Bogdanov, A. G., Brandt, D., Brown, J. M. C., Burkhardt, H., Canal, Ph., Cano-Ott, D., Chauvie, S., Cho, K., et al., "Recent developments in Geant4," Nuclear Instruments and Methods in Physics Research Section A: Accelerators, Spectrometers, Detectors and Associated Equipment **835**, 186–225 (2016).
[23] Matt Newville., "XrayDB," <https://github.com/xraypy/XrayDB/> (17 November 2023).
[24] Poludniowski, G., Landry, G., DeBlois, F., Evans, P. M. and Verhaegen, F., "SpekCalc: a program to calculate photon spectra from tungsten anode x-ray tubes," Physics in Medicine and Biology **54**(19), N433–N438 (2009).
[25] White, D. R., Griffith, R. V. and Wilson, I. J., "Report 46," Journal of the International Commission on Radiation Units and Measurements **os24**(1), NP-NP (1992).

APPENDIX A

A.1 Supplementary Methods – Object and material definitions

This section details which soft tissue definition we used, and how we varied the electron density or the effective atomic number while keeping the other parameter fixed.

For the soft tissue insert, the chemical composition, and thus Z_{eff}, was changed along a multidimensional line in the space of chemical composition, with the origin being the composition of water and passing through the point of the average soft tissue composition of humans (average of soft tissue compositions "Adult ICRU-44 (male)" and "Adult ICRU-44 (female)" as listed in ICRU report[25] 46), where the average human soft tissue composition has the following mass fractions: H=0.1055, C=0.2855, N=0.0255, O=0.5745, Na=0.001, P=0.002, S=0.0025, Cl=0.0015, K=0.002.

The multidimensional line was parametrized via a parameter α such that for $\alpha = 0$, the chemical composition equals water and for $\alpha = 1$ it equals the average soft tissue stated above. Hence, for a given value of α the mass fraction f_i of element i is determined as follows:

$$f_i = f_{i,\text{H2O}} + \alpha \cdot (f_{i,\text{ST}} - f_{i,\text{H2O}}) \tag{A1}$$

where $f_{i,\text{H2O}}$ and $f_{i,\text{ST}}$ denote the mass fraction of element i in water and the average human soft tissue specified above, respectively.

For determining the partial derivative w.r.t. Z_{eff}, α was set to the values $[0, 1, 2, 3, 4] \cdot 0.291$, which changes Z_{eff} in steps of approximately 1 %; the mass density of each resulting composition was adjusted such that its value for ρ_{elec} equals the electron density of water. The such obtained tissue definitions were then used for evaluating the partial derivative w.r.t. Z_{eff}. See Table A1 for the resulting elemental compositions and mass densities.

For determining the partial derivative w.r.t. ρ_{elec}, the chemical composition was fixed at $\alpha = 2 \cdot 0.291$, the mass density was adjusted such that its electron density equals the density of water, and the electron density was changed in steps of 1 %.

Table A1: Elemental compositions in weight fractions (in percent) of the tissues used.

	Soft tissue at $\theta_{Z_{\text{eff}}} - 2\Delta\theta_{Z_{\text{eff}}}$, $\alpha = 0$	Soft tissue at $\theta_{Z_{\text{eff}}} - \Delta\theta_{Z_{\text{eff}}}$, $\alpha = 1 \cdot 0.291$	Soft tissue at $\theta_{Z_{\text{eff}}}$, $\alpha = 2 \cdot 0.291$	Soft tissue at $\theta_{Z_{\text{eff}}} + \Delta\theta_{Z_{\text{eff}}}$, $\alpha = 3 \cdot 0.291$	Soft tissue at $\theta_{Z_{\text{eff}}} + 2\Delta\theta_{Z_{\text{eff}}}$, $\alpha = 4 \cdot 0.291$	Cortical bone
H	11.190	11.004	10.817	10.631	10.445	3.4
C	0	8.308	16.616	24.924	33.232	15.5
N	0	0.0742	1.484	2.226	2.968	4.2
O	88.81	79.684	70.559	61.433	52.307	43.5
Na	0	0.029	0.058	0.087	0.116	0.1
Mg	0	0	0	0	0	0.2
P	0	0.058	0.116	0.175	0.233	10.3
S	0	0.073	0.145	0.218	0.291	0.3
Cl	0	0.044	0.087	0.131	0.175	0
K	0	0.058	0.116	0.175	0.233	0
Ca	0	0	0	0	0	22.5
Mass density [g/cm^3]	1.000000	1.001791	1.003589	1.005393	1.007203	1.920

APPENDIX B

B.1 Supplementary Results – Number of photons emitted by source

Table B1 lists the number of photons emitted by the source in the kVp-switching setup for various source voltage pairs and current ratios in order to reach the desired deposited cumulative (i.e., combined deposition by high and low energy spectra) target energy in the phantom.

Table B1: Number of photons n_γ emitted by the source in the kVp-switching setup for various source voltage pairs and current ratios in order to reach the desired deposited cumulative target energy in the phantom (LE: low energy; HE: high energy).

	80 / 140 kVp		100 / 140 kVp		120 / 140 kVp		80 / 120 kVp	
Current ratio (I_{LE}/I_{HE})	$n_{\gamma,LE}$	$n_{\gamma,HE}$	$n_{\gamma,LE}$	$n_{\gamma,HE}$	$n_{\gamma,LE}$	$n_{\gamma,HE}$	$n_{\gamma,LE}$	$n_{\gamma,HE}$
10:1	704744	285580	801467	174592	839337	117620	776775	224619
9:1	681641	306909	785198	190054	827783	128890	757092	243252
8:1	654810	331681	765767	208519	813779	142548	733846	265256
7:1	623267	360804	742154	230959	796455	159444	705978	291638
6:1	585651	395534	712846	258812	774473	180884	671953	323846
5:1	540022	437661	675499	294303	745660	208986	629481	364052
4:1	483516	489831	626282	341075	706249	247425	574967	415656
3:1	411714	556123	558465	405522	649071	303191	502447	484305
2:1	317437	643166	459050	499999	558620	391410	401232	580118
1:1	188170	762513	299241	651869	393931	552034	250093	723190
1:2	103707	840494	176412	768595	247814	694545	142635	824912
1:3	71578	870158	125073	817383	180764	759940	99768	865491

Table B2 lists the number of photons emitted by the source in the PCD setup for various source voltages in order to reach the desired deposited target energy in the phantom.

Table B2: Number of photons n_γ emitted by the source for various source voltages of the PCD setup.

Source voltage [kVp]	n_γ
80	1014121
100	984925
120	960047
140	936078